New Journal of Physics
The open access journal at the forefront of physics
Deutsche Physikalische Gesellschaft DPG IOP Institute of Physics

PAPER • OPEN ACCESS

Double edge-diffraction mediated virtual shadow for distance metrology

To cite this article: George Y Chen *et al* 2018 *New J. Phys.* **20** 103029

New Journal of Physics
The open access journal at the forefront of physics

Deutsche Physikalische Gesellschaft DPG
IOP Institute of Physics
Published in partnership with: Deutsche Physikalische Gesellschaft and the Institute of Physics

PAPER

Double edge-diffraction mediated virtual shadow for distance metrology

CrossMark

OPEN ACCESS

RECEIVED
10 June 2018

REVISED
25 September 2018

ACCEPTED FOR PUBLICATION
2 October 2018

PUBLISHED
23 October 2018

George Y Chen[1], **Timothy Lee**[2], **Yvonne Qiongyue Kang**[1], **Tanya M Monro**[1] and **David G Lancaster**[1]

[1] Laser Physics and Photonic Devices Laboratories, School of Engineering, University of South Australia, Mawson Lakes, SA 5095, Australia
[2] Optoelectronics Research Centre, University of Southampton, Southampton, SO17 1BJ, United Kingdom

E-mail: george.chen@unisa.edu.au

Keywords: diffraction, distance, metrology, measurement, double, edge

Abstract

We report a form of double edge-diffraction (DED) for the first time, in which successive diffractive effects between two opaque objects leads to a virtual shadow of one object that protrudes from the shadow of the other. Analogous to classic edge and slit diffractions, the method to observe DED is simple, yet its effect is intriguingly different. Existing sensing techniques cannot measure the distance of highly reflective or absorptive opaque objects. To address this problem in certain scenarios, we propose a new technique based on DED that is the first to work for all opaque objects with well-defined edges.

1. Introduction

Diffraction is a well-known phenomenon in physics associated with bending of waves around the edge of an object or aperture. Although diffraction [1] can be experienced by both transverse electromagnetic waves (e.g. light) [2] and transverse/longitudinal mechanical waves [3], the most obvious cases involve visible light. To observe the effects of diffraction, the classic examples comprise single or multiple slits/circular apertures [4] or a single edge of an object [5]. The resulting effect can be observed as a diffraction pattern from the interfering wavefronts [6].

We report a specific form of double edge-diffraction (DED) for the first time, which is a diffractive effect that leads to a new type of virtual shadow, as shown in figure 1. Although the physics behind DED is simple, it is fundamental to this field, as it complements the classic diffractive effects. DED can be observed in its pure form, by using a collimated light source and two opaque objects (e.g. absorptive, reflective or forward/side-scattering) positioned so their shadows are in close proximity, as done in this work. The observed virtual shadow of one object that protrudes from the shadow of another object is diffractive in origin, and as we shall show, it can be modeled using diffraction theory.

A visually similar shadow inversion effect has previously been reported as the shadow blister effect (SBE) [7]. In SBE, a divergent light source illuminating two objects casts penumbras around their darker umbra shadows. When these penumbras overlap, their crossing of rays leads to shadow inversion, or 'blistering'. On a sunny day, one can readily observe such effects in shadows on the ground. The effect is geometric and has been modeled using ray optics [7]. However, this explanation is incomplete as it overlooks the diffractive contribution of DED, which is explored in this work. More importantly, we demonstrate that when diffraction is taken into account, DED exhibits different effects and can occur even if penumbra are not cast, by using a plane wave, collimated beam, or point source. In effect, the medium- to far-field diffraction fringes can play a role somewhat similar to the penumbra, with overlapping fringes manifesting shadow inversion.

Distance metrology is important for a number of applications spanning from automotive/aircraft to astronomy. Longitudinal distance (z_{long}) measurement of opaque objects within remote environments suffer from limitations in which highly reflective or absorbing objects are difficult to detect with conventional techniques (e.g. time of flight of back-scattered light) [8–12]. Overcoming this hurdle will enable a more

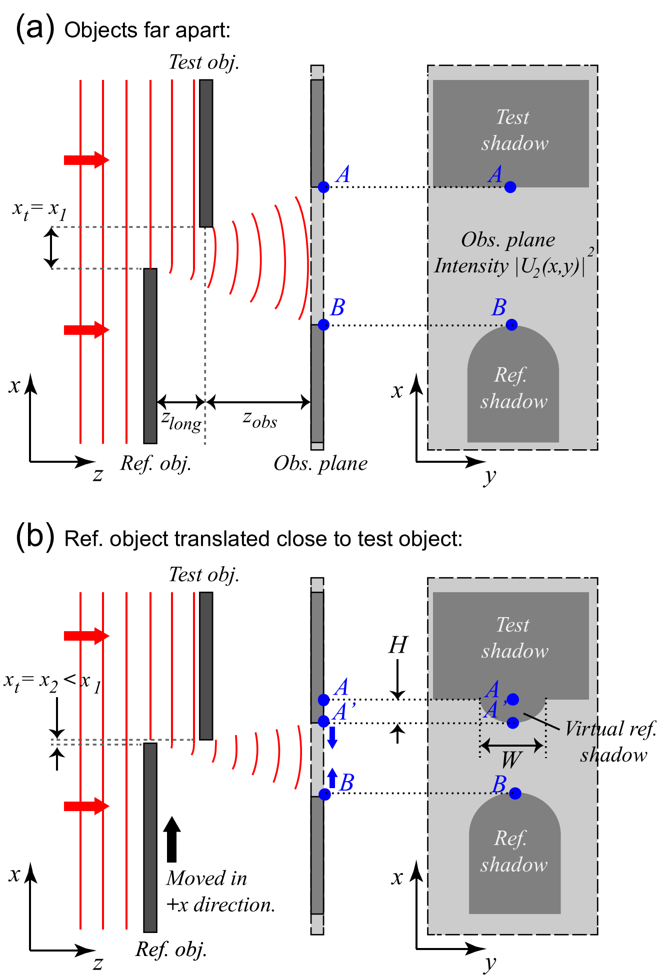

Figure 1. Illustration of double edge-diffraction with two opaque objects placed (a) far apart; or (b) closed together. The objects are thin or have sharp edges in contact with light. Not drawn to scale.

comprehensive ability to measure the distance of objects. The SBE also produces a distortion of the shadow from two close objects, but relies on diverging rays, and thus cannot provide long-distance measurements without significant fading [13].

To address the problem of the inability to measure all opaque objects, we investigate DED and then demonstrate its ability to measure z_{long} that is the first technique to work in certain scenarios for all opaque objects with at least one well-defined edge. It works because in transmission (i.e. doubled ended) rather than reflection (i.e. practical single-ended), diffraction occurs regardless of the object being absorptive, reflective or forward/side-scattering [2].

2. Principles

DED can be implemented by using any light source in conjunction with two opaque objects shown in shown in figure 1(a). Along the longitudinal direction from the light source to the observation plane, one object must be nearer to the light source than the other object in order to facilitate successive edge diffractions. Transverse to this direction, the edges of the two objects need to be close (e.g. $<$1 mm for visible wavelengths, z_{long} is $\sim$20 cm, and the observation distance (z_{obs}) is $\sim$25 cm). For rough edges, the spatial variation in the edge profile must not exceed the size of the virtual reference shadow, in order for the latter to be distinguishable. The light source can emit light of narrow spectral linewidth or broad spectral bandwidth of any divergence angle. For the simplest case that avoids the SBE due to penumbra, we will consider a collimated light source of a single wavelength. Fulfilling these simple conditions will result in the shadow of the object nearer to the light source manifesting a highly visible virtual reference shadow that protrudes from the shadow of the other object, as shown by figure 1(b).

Table 1. Summary of the changes in the virtual reference shadow in response to changes in object positions.

Parameter change	Height (H) of virtual reference shadow	Width (W) of virtual reference shadow
Increase z_{long}	Negligible change	Increase
Decrease z_{obs}	Decrease	Negligible change
Both	Decrease	Increase

As we decrease the transverse distance (x_t) between the two opaque objects, their shadows rapidly converge towards each other due to the narrow passage of light supporting diffraction (i.e. makes shadows seem farther apart than the real objects) experiencing a squeeze. Diffraction around the reference object in front is not affected as much, because the incoming light is not blocked and can bend around the test object. However, the test object behind it (i.e. nearer to the observation plane) has its light source increasingly counter-diffracted towards the opposite transverse side. Owing to the transverse spatial displacement (x_t), increasingly higher diffraction angles of wavefronts coming from the reference object are subdued with increasingly lower diffraction angles at the test object. Therefore, the collapse of the light gap (i.e. the distance A'B in figure 1(b)) begins from the test object side, and the test shadow manifests an extension in the form of a virtual shadow as a function of the reference shadow.

As we increase z_{long} while keeping z_{obs} constant, the width of the virtual reference shadow can be observed to stretch (see table 1 and figure 8(a)). Owing to z_{long} elongation, the diffracted wavefronts around the edge of the reference object shown in figure 1(b) gradually experience more bending, and thus the test object encounters increasingly higher diffraction angles of wavefronts caused by the reference object. The height of the virtual reference shadow is not noticeably stretched with increasing z_{long}, because the inner edge of the test object now intercept wavefronts of lower diffraction-angles coming from the reference object, which increasingly offsets the previous effect.

As we decrease z_{obs} while keeping z_{long} constant, the height of the virtual reference shadow can be observed to compress (table 1 and figure 8(b)) due to two complementary factors. First, diffracted light spreads out over increasing zobs, which transversely recedes the baseline of the two shadows shown in figure 1(b). Second, diffracted light passing around the inner edge of the test object could all be shifting towards the reference shadow with increasing zobs due to stronger counter-diffraction from the reference object with a narrower x_t. Note that diffraction angles increase with increasing distance, and in most cases cannot be fully compensated by a counter-diffraction within the range of zobs hosting non-overlapping shadows.

For the purpose of z_{long} measurement, it is practical to fix the position of the reference object and the camera, and monitor the relative position of the test object. An object with a known shape must be used as the reference in order to determine the extent of transformation the virtual reference shadow has undergone. The transformation in this case is a combination of the changes in z_{long} and z_{obs}. This results in an amplified change in the ellipticity of the virtual reference shadow.

3. Experimental setup

The experimental demonstration of DED as well as its application in the measurement of z_{long} can be achieved using the configuration shown in figure 2. To interrogate the two objects, a laser source (Thorlabs HNLS008R) emitting unpolarized narrow spectral linewidth light at 633 $\pm$ 0.5 nm wavelength was used. Unpolarized can be used since light propagation is polarization independent for low-intensity light through air over the distances involved. Polarization-dependent effects could play a role if light propagates through an anisotropic structure, or is tightly focused with high intensity leading to nonlinear effects [14]. A pair of plano-convex lenses (30 and 300 mm focal length) were used to expand and collimate the beam to 10.0 $\pm$ 0.05 mm diameter (D4σ fitting of beam diameter). An anodized (i.e. black) aluminum piece featuring a rounded end of 6.0 $\pm$ 0.05 mm diameter was chosen as the reference object, and mounted on a linear translation stage aligned parallel to the beam. An anodized aluminum block with a flat side much longer than the beam diameter was selected as the test object, and mounted on a slider resting on a rail. Both objects were slightly tilted such that their edges interacting with the beam are relatively sharp, and thus the diffraction strength was enhanced by the knife-edge effect [15]. To capture the shadows across the observation plane, a charge-coupled-device (CCD) camera (Ophir Spiricon BGS-USB-SP928) was used.

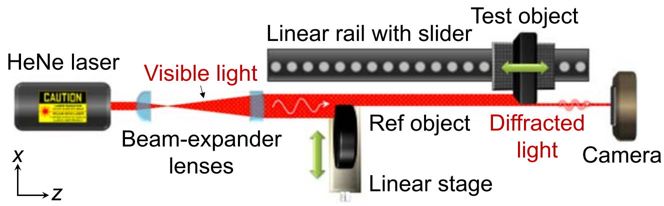

Figure 2. Experimental setup for effect observation and z_{long} measurement.

4. Results and discussions

To quantify the shift of the virtual shadow as a function of x_t, the reference object was incrementally shifted towards the test object, while their shadows were captured by the CCD camera. z_{long} was fixed at 191 $\pm$ 0.5 mm, and z_{obs} is fixed at 251.5 $\pm$ 0.5 mm. Figure 3 reveals that as the reference object was translated towards the test object, a virtual shadow emerged from the test shadow that is an inverted form of the reference shadow. To increase the visibility of the shadows, an intensity normalization followed by a threshold filter (50%) were applied. The geometry of the virtual reference shadow was preserved while it shifted towards the incoming reference shadow, before the two shadows completely merged. During this process, a diffraction pattern can be seen in the background from both the reference and test objects, which was attributed to the coherent diffracted waves interfering with each other at the observation plane.

To quantify the evolution of the virtual shadow as a function of z_{long}, the test object was incrementally shifted along the rail away from the reference object, while their shadows were monitored by the CCD camera. x_t was fixed at 80 $\pm$ 10 μm, and the observation plane is fixed at 442.5 $\pm$ 0.5 mm from the edge of the reference object. Figure 4 shows that as the test object was translated away from the reference object (i.e. increase in z_{long}, decrease in z_{obs}), the virtual reference shadow gradually transformed from a tall and sharp ellipse to a short and broad ellipse. To increase the visibility of the shadows, an intensity normalization followed by a threshold filter (1.5%) were applied, followed by an edge filter to obtain shadow outlines for easier geometry calculations.

In a practical measurement environment, x_t could be adjusted in real-time, from analyzing the linear translation needed to induce a virtual shadow. For straight edges, z_{long} can be loaded from calibrated data. For curved edges, the simulation model could possibly operate in real-time to extract z_{long}, from importing the geometry of the test shadow to obtain the best fit of the measured data.

The sensitivity derived from figure 4 shown in figure 5(a) varies from 0.008 to 0.075 mm^{-1} as z_{long} increases from 1 to 381 mm, from taking the slope at each data point of the relationship between z_{long} and the corresponding ellipse ratio (i.e. width divided by height from the baseline) of the virtual reference shadow. It was found that the relationship can be empirically described by a 3rd order polynomial equation, which reflects the interplay of the two relationships associated with the changing distances between the reference object, test object and the camera.

The ellipticity-ratio errors due to system noise, image-processing uncertainties and measurement repeatability errors range from $\pm$0.005 to $\pm$0.545, which is larger for smaller dimensions. The detection limit or accuracy shown in figure 5(b) grows from 0.223 to 9.514 mm as z_{long} increases from 1 to 381 mm, from dividing the ellipticity-ratio errors by their corresponding sensitivity. This means for decreasing z_{long} the technique is expected to resolve ever shorter distances due to the increasing height of the virtual reference shadow. It can be seen that the detection limit or accuracy is approximately constant at ~4.5 mm between 100 to 350 mm. The corresponding error bars for ellipticity ratio and z_{long} ($\pm$0.5 mm) are included in figure 5.

Although the demonstrated range of measurable z_{long} range from 1 to 381 mm, the actual dynamic range is anticipated to be much wider. The upper limit of the response/recovery times are governed by the frame rate of the camera, which in this case yields 77 ms.

To increase the sensitivity, the diffraction strength must be heightened (i.e. using longer wavelength [16]), which amplifies the change in the virtual reference shadow with varying z_{long} such that it is more measurable. The detection limit can be lowered, or accuracy can be improved by using a higher-resolution camera, which lowers the width/height errors. To increase the dynamic range for long-distance measurements, the diffraction strength must be lowered (i.e. using shorter wavelength), which reduces the change in the virtual reference shadow with varying z_{long} such that the height of the virtual reference shadow is still measurable after decreasing over a long z_{long}. The dynamic range can be further increased by increasing z_{obs}, which elongates the height of the virtual reference shadow at all z_{long} such that it is still measurable after decreasing over a long z_{long}. Since there is a conflicting requirement of wavelength, there is a trade-off between sensitivity/detection limit/accuracy and

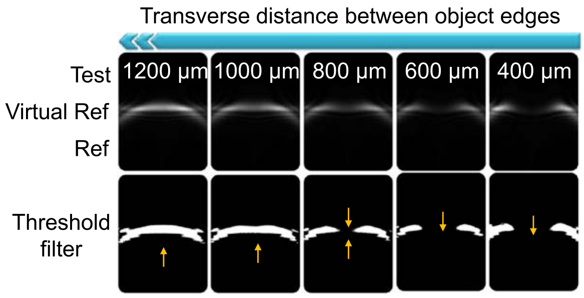

Figure 3. Measured shift in the virtual reference shadow as a function of x_t, when z_{long} is 191 mm, and z_{obs} is 251.5 mm. For scale, the width of each image is 5.3 mm.

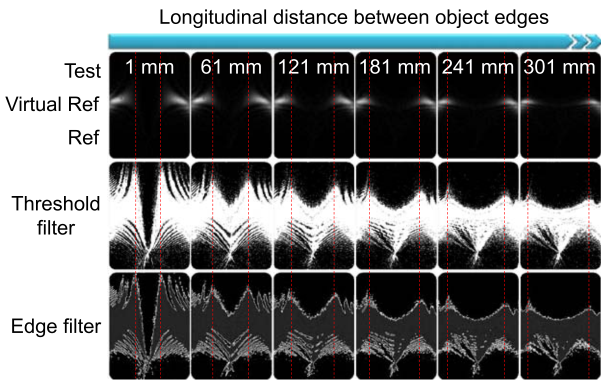

Figure 4. Measured evolution of the virtual reference shadow as a function of z_{long}, when x_t is 80 μm, and the observation plane is 442.5 mm from the edge of the reference object.

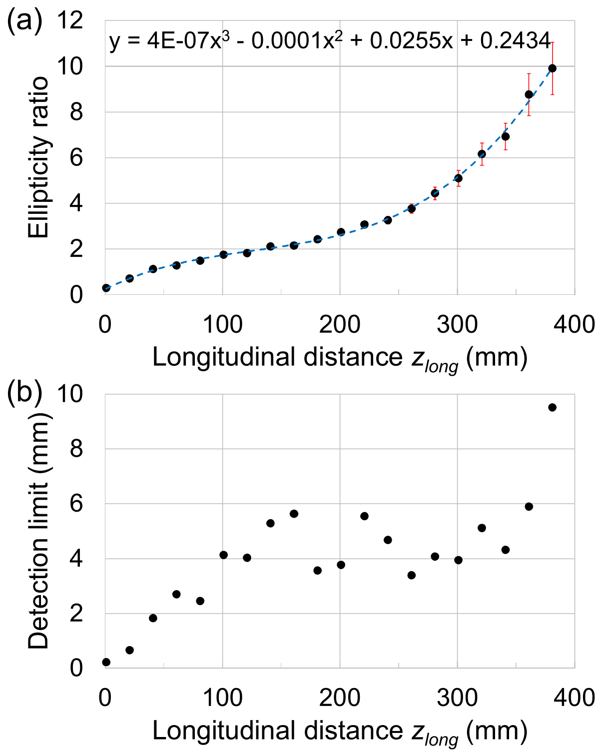

Figure 5. Measured relationship between: (a) the ellipticity ratio and z_{long}, with 3rd order polynomial fit and error bars; and (b) the detection limit and z_{long}.

dynamic range. Optimization of the wavelength will deliver a good balance of the sensor parameters. However, this trade-off can be avoided by just increasing z_{obs}.

5. Simulations

To verify the origin of DED and study this diffractive effect further, we modeled its behavior by numerically solving the Rayleigh–Sommerfeld (RS) diffraction integral of the first kind [17], which states that for a given source field $U_1(x', y')$, the observed field $U_2(x, y)$ at a distance z away can be calculated from the RS integral:

$$U_2(x, y) = \frac{z}{j\lambda}\int\int_{-\infty}^{-\infty} U_1(x', y')\frac{\exp(jkr_{12})}{r_{12}^2}\mathrm{d}x'\mathrm{d}y', \tag{1}$$

where λ is the wavelength, $k = 2\pi/\lambda$ is the wavenumber, and r_{12} is the distance between a point on the source plane and the observation plane, assumed to be parallel to each other, such that:

$$r_{12} = \sqrt{(x - x')^2 + (y - y')^2 + z^2}. \tag{2}$$

In our case, the situation simplifies since the source and observation planes are flat (i.e. planar) and parallel, so equation (1) becomes a convolution integral expressed as:

$$U_2(x, y) = \int\int_{-\infty}^{\infty} U_1(x', y')h(x - x', y - y')\mathrm{d}x'\mathrm{d}y', \tag{3}$$

$$= U_1(x, y) * h(x, y), \tag{4}$$

where $h(x, y)$ can be considered as the RS impulse response:

$$h(x, y) = \frac{z}{j\lambda}\frac{\exp(jkr)}{r^2}, \tag{5}$$

$$r = \sqrt{x^2 + y^2 + z^2}. \tag{6}$$

Applying the Fourier convolution theorem to (4) and (5), we obtain:

$$U_2(x, y) = \mathfrak{F}^{-1}\{\mathfrak{F}\{U_1(x, y)\}\mathfrak{F}\{h(x, y)\}\}. \tag{7}$$

Equation (7) can be calculated numerically using the 2D fast Fourier transform in MATLAB. In the implementation, the source and observation fields are represented as matrices of the same size, aligned such that they share the same x–y axes.

We simplify the input field as a plane wave. This is a reasonable approximation since the beam in the experiment was well collimated with a diameter of 1 cm, which considerably exceeds the millimeter-scale region of interest where the shadows interact. The reference and test objects are modeled as amplitude masks (i.e. same dimensions as in experiment), with zero transmission where the object blocks the beam, and full transmission elsewhere. The beam propagation is conducted in two steps: (1) from the reference object to the test object; and (2) from the test object to the observation plane. Since using the 2D FFT to solve the RS integral becomes computationally intensive over large areas, we restrict the field to an area of 3×3 cm using 10^4 points for each direction, which ensures a resolution more than sufficient to discern the diffraction patterns. The simulated evolution of a virtual shadow as a function of z_{long} is shown in figure 6, which shares the conditions and processing of figure 5.

The sensitivities derived from figure 6 shown in figure 7 vary from 0.013 to 0.172 mm^{-1} as z_{long} increases from 1 to 381 mm. This trend mirrors that of the experimental data shown in figure 5(a), judging by the shape or the polarity of the polynomial coefficients, which confirms the origin of DED. The discrepancies in magnitude could be attributed to: (a) the different thicknesses of the edge in experiment (i.e. sharp edge) and the simulation (i.e. infinitesimally thin edge); (b) the different input intensity profile of collimated light between the experiment (i.e. Gaussian, approximately uniform in the region of interest) and the simulation (i.e. plane wave). The ellipticity-ratio errors due to image-processing uncertainties ranges from ± 0.010 to ± 1.833, which is larger for smaller dimensions/number of pixels. The corresponding error bars for the ellipticity ratio are included in figure 7.

The impact of individually changing z_{long} and z_{obs} is simulated in figure 8, with the same conditions and processing of figure 4. Figure 8(a) shows that increasing only z_{long} increases the width of the virtual reference shadow, with negligible decrease in height. Figure 8(b) shows that increasing only z_{obs} increases the height of the virtual reference shadow, with negligible increase in width. In each case, one distance is varied while the other is fixed at 200 mm. The width/height errors based on image-processing uncertainties is ± 10 μm. The corresponding error bars for the width/height are included in figure 8. Overall, it shows excellent agreement with the experimental observations and table 1.

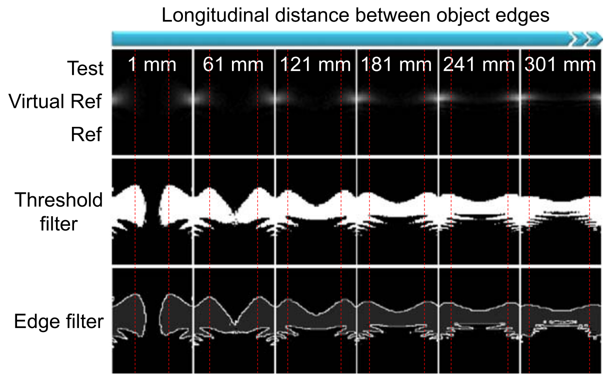

Figure 6. Simulated evolution of the virtual reference shadow as a function of $z_{\rm long}$, when x_t is 80 μm, and the observation plane is 442.5 mm from the edge of the reference object.

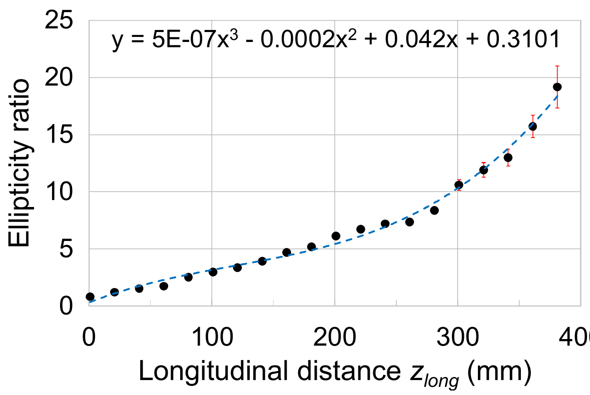

Figure 7. Simulated relationship between the ellipticity ratio and $z_{\rm long}$, with 3rd order polynomial fit and error bars.

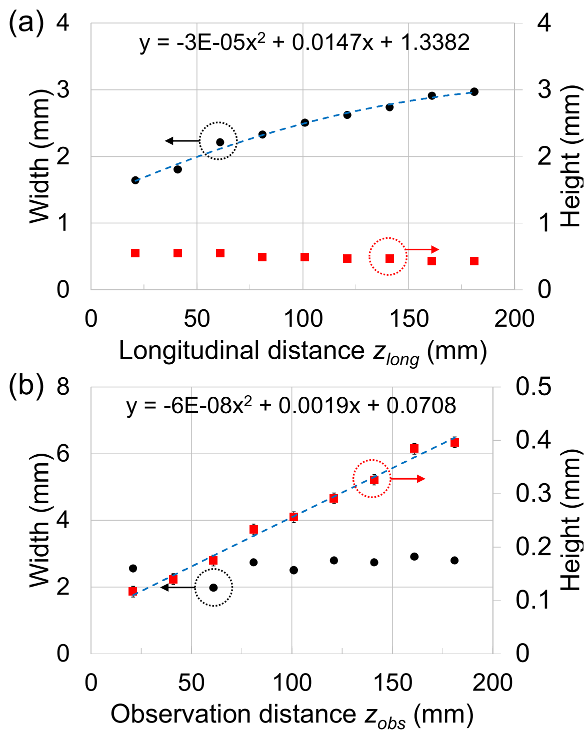

Figure 8. Simulated relationship between: (a) width/height of the virtual reference shadow and $z_{\rm long}$, when $z_{\rm obs}$ is 200 mm; and (b) width/height and $z_{\rm obs}$, when $z_{\rm long}$ is 200 mm; with 2nd order polynomial fit and error bars. x_t is 80 μm in both cases.

6. Discussion

A speculated application that could benefit from this diffractive effect include the separation-distance management of a swarm of miniature stealth drones. To reduce the chance of detection, such drones are almost fully covered with a highly absorbing or reflective material. Global positioning systems do not function accurately for tight spaces (e.g. <0.5 m) nor shielded environments. Measuring separation distances by analyzing the signal strength alone is not a reliable method due to unpredictable attenuation from environmental factors. Instead, DED can be employed with the drones' onboard collimated light source and camera in conjunction with their standard navigation sensors to maintain safe separation distances with each other during group formation and tight maneuvers.

Another potential application is the measurement of size, shape, velocity and mass/density of particles in optofluidic devices for a wide variety of chemical applications using a collimated light source and a camera. The mass or density of a particle is related to its 3D position in a fluidic channel with a non-zero flow velocity, due to the equilibrium that balances the hydrodynamic lift and buoyant weight [18]. Conventional shadow-based imaging systems can infer the 2D position of a particle without the depth information, if the channel is not located near a side of a flat and wide optofluidic substrate [19]. Advantageously, DED can reveal the 3D position from the standard top-down view to infer the mass/density. This enhancement technique could be applied to measure a wide range of particles types including bubbles, liquid droplets, solid particles and any object with a well-defined contour.

It may also be possible to perform distance measurements of single undersea objects (e.g. submarine) with acoustic waves [20], since longitudinal waves can also experience diffraction. Additionally, this technique could be further developed to supplement internal imaging of solid materials (e.g. rocks) with additional spatial information.

7. Conclusion

We report DED for the first time. This fundamental diffractive effect manifests a virtual shadow that is a function of the shape of the object nearest to the light source, and a function of the longitudinal distance to the object farthest from the light source. This diffractive effect was previously overlooked as it can produce a result visually similar to that of the ray-optics-based SBE [6]. DED can be observed alone using a collimated beam, or as the unexplained part of the SBE using diverging rays. Exploiting this new phenomenon led to the development of a new technique for measuring the longitudinal distance of all opaque objects in certain scenarios with at least one well-defined edge. However, this technique is based on transmission rather than reflection, which limits the cases in which it can be practically used. The sensitivity ranges from 0.008 to 0.075 mm^{-1}, and the detection limit or accuracy varies from 0.223 to 9.514 mm, as the longitudinal distance (z_{long}) increases from 1 to 381 mm.

Acknowledgments

Tanya M Monro acknowledges the support of an ARC Georgina Sweet Laureate Fellowship.

Conflict of interest

The authors declare no conflict of interest.

ORCID iDs

George Y Chen https://orcid.org/0000-0002-2469-9093
Timothy Lee https://orcid.org/0000-0001-9665-5578
Yvonne Qiongyue Kang https://orcid.org/0000-0003-2533-5213
Tanya M Monro https://orcid.org/0000-0003-0063-8293
David G Lancaster https://orcid.org/0000-0002-1299-8600

References

[1] de Abajo F J G, Estrada H and Meseguer F 2009 Diacritical study of light, electrons and sound scattering by particles and holes *New J. Phys.* **11** 093013
[2] Bekefi G 1953 Diffraction of electromagnetic waves by an aperture in a large screen *J. Appl. Phys.* **24** 1123
[3] Assier R C and Peake N 2012 On the diffraction of acoustic waves by a quarter-plane *Wave Motion* **49** 64

[4] Li Y, Wang X, Zhao H, Kong L, Lou K, Gu B, Tu C and Wang H 2012 Youngs two-slit interference of vector light fields *Opt. Lett.* **37** 1790
[5] Borghi R 2016 Catastrophe optics of sharp-edge diffraction *Opt. Lett.* **41** 3114
[6] Liu D, Zhang Y, Wen J, Chen Z, Wei D, Hu X, Zhao G, Zhu S N and Xiao M 2014 Diffraction interference induced superfocusing in nonlinear talbot effect *Sci. Rep.* **4** 6134
[7] Lock J A 1998 Ray theory analysis of the shadow blister effect *Appl. Opt.* **37** 1573
[8] Xiaoli D and Katuo S 1998 High-accuracy absolute distance measurement by means of wavelength scanning heterodyne interferometry *Meas. Sci. Technol.* **9** 1031
[9] Lee J, Kim Y, Lee K, Lee S and Kim S 2010 Time-of-flight measurement with femtosecond light pulses *Nat. Photon.* **4** 716
[10] Schütt H H, Baier F and Fleming R W 2016 Perception of light source distance from shading patterns *J. Vis.* **16** 9
[11] Fu W, Yan F, Chen K and Ren Z 2015 Scene distance measurement method based on light field imaging *Appl. Opt.* **54** 6237
[12] Ito F, Fan X and Koshikiya Y 2012 Long-range coherent OFDR with light source phase noise compensation *J. Lightwave Technol.* **30** 1015
[13] Chugui Y V, Yahovenko N A and Yaluplin M D 2010 A novel method for measurement of small opaque objects using fraunhofer diffraction in divergent light *Meas. Sci. Technol.* **21** 054012
[14] Hube C, Orlov S, Banzer P and Leuchs G 2013 Corrections to the knife-edge based reconstruction scheme of tightly focused light beams *Opt. Express* **21** 25069
[15] Kumar R, Kaura S K, Sharma A K, Chhachhia D P and Aggarwal A K 2007 Knife-edge diffraction pattern as an interference phenomenon: an experimental reality *Opt. Laser Technol.* **39** 256
[16] Gao P *et al* 2012 Autofocusing based on wavelength dependence of diffraction in two-wavelength digital holographic microscopy *Opt. Lett.* **37** 1172
[17] Voelz D G 2011 *Computational Fourier Optics* (Bellingham, WA: SPIE Press)
[18] Joseph D D and Ocando D 2002 Slip velocity and life *J. Fluid Mech.* **454** 263
[19] Card J B A and Jones A R 2003 Development of a method for the measurement of particle size and velocity based on projection onto a variable frequency grating *Part. Part. Syst. Charact.* **20** 259
[20] Su D, Ulapane N and Vijerathna B 2015 An acoustic sensor based novel method for 2D localization of a robot in a structured environment *10th ICIEA* vol 2024 (https://doi.org/10.1109/ICIEA.2015.7334446)